Draft version January 21, 2025
Typeset using LaTeX **twocolumn** style in AASTeX62

JWST spectroscopy reveals low AGN incidence in star-forming galaxies at z∼3

Gena Levin,[1] Tucker Jones,[1] and Ivana Barišić[1]

[1] *Department of Physics and Astronomy, University of California, Davis, 1 Shields Avenue, Davis, CA 95616, USA*

ABSTRACT

Every massive galaxy hosts a central supermassive black hole (SMBH), yet their origins are unknown and their co-evolution with their host galaxies is poorly understood. We utilize pseudo-integral field spectroscopy from slit-stepping observations with JWST's NIRSpec MSA to investigate the incidence of active galactic nuclei (AGN) around the cosmic time associated with the peak of star formation and black hole accretion. Our sample consists of 42 photo-z-selected star-forming galaxies at z∼3 within the Extended Groth Strip, constructed to span a range of stellar masses. We analyze Baldwin, Phillips & Terlevich (BPT) and WHAN diagnostics for 18 and 30 of the 42 galaxies respectively, those with detection of the requisite emission lines, to categorize the ionization in each as driven by star formation or AGN activity. Moreover, the spatially resolved data provide excellent sensitivity to AGN by allowing us to isolate the emission lines from the central kpc. We find one target that exhibits an AGN signature according to both diagnostics, and two more potential AGN. These AGN fall within the most massive ∼10% of galaxies in our sample. This result is consistent with the trend established at z∼2, that AGN detections are mass-dependent, with higher-mass galaxies being much more likely to have them (e.g., Genzel et al. 2014). Future work will examine our result in the context of multi-wavelength censuses of AGN.

1. INTRODUCTION

Supermassive black holes (SMBHs), defined as having masses greater than $\sim 10^6$ times the mass of the Sun ($M_\odot$), are ubiquitous in the center of massive galaxies. However, the origins of SMBHs and the ways they get to be so massive remain elusive. Decades of work (reviewed in e.g. Rees 1978; Volonteri 2010; Inayoshi et al. 2020) reveal a few leading scenarios for SMBH seeding, including the gravitational collapse of low metallicity, first generation stars forming light $\sim 10^{2-3}$ $M_\odot$ seeds by z∼20 (e.g. Madau & Rees 2001; Tan & McKee 2004; McKee & Tan 2008), and the direct collapse of primordial gas clouds into supermassive stars that form $\sim 10^{4-5}$ seeds by z∼ 10 (e.g. Bromm & Loeb 2003; Begelman et al. 2006; Montero et al. 2012). From these seeds, SMBHs must grow some orders of magnitude across cosmic time to reach the masses we observe. Recently, the discovery of SMBHs as massive as 10^{10} $M_\odot$ by z∼6-7 (reviewed in e.g. Fan et al. 2023) suggest that seeds may start more massive and grow more rapidly than previously thought.

SMBHs are thought to grow via mergers and accretion. When they are actively accreting material, we refer to them as active galactic nuclei (AGN). AGN are characterized by material rapidly falling onto a black hole that generates very high-energy radiation. This material forms an accretion disk around the black hole, shrouded by a dusty torus, as pictured in Figure 1. AGN emission is detected across the electromagnetic spectrum, from radio to gamma waves. Comparable to the rest-frame optical emission lines that characterize star formation are those from the narrow line region (NLR) and the broad line region (BLR). Both the NLR and BLR harbor gas that is photoionized by black hole accretion, where the NLR refers to the lower-density gas located above and below the dusty torus, moving at 300-1000 km s^{-1}, and the BLR refers to the higher-density gas between the SMBH and the torus, moving at > 1000 km s^{-1}.

In the local universe, at z∼0, relationships between the mass of a SMBH and its host galaxy are well defined, where SMBH mass is highly correlated with the bulge mass (Magorrian et al. 1998), stellar velocity dispersion (e.g. Ferrarese & Merritt 2000; Gebhardt et al. 2000), and luminosity (e.g. Kormendy & Richstone 1995) of its host (e.g. reviewed in Kormendy & Ho 2013). This suggests a link between SMBH growth and galaxy growth, where AGN activity plays a role in modulating star formation as galaxies evolve and develop structure as defined by the Hubble sequence (e.g. reviewed in Zhuang & Ho 2023). The interplay between the SMBH and its host is referred to as SMBH-galaxy co-evolution. The peaks of galaxy growth via star formation and black hole growth via accretion both occur

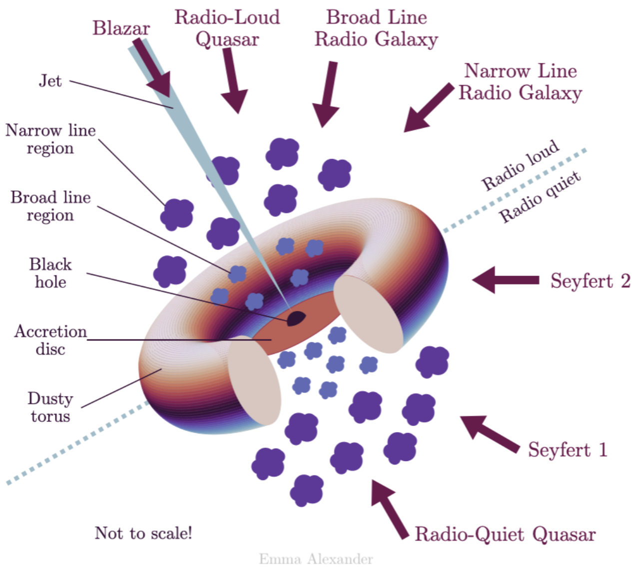

Figure 1. Diagram of an active galactic nucleus (AGN), adapted by Alexander (2022), showing the unified model of AGN from Urry & Padovani (1995). Diagram shows a black hole surrounded by an accretion disk and a dusty torus, with indicators for different regions of ionization. Bold arrows indicate AGN classification based on viewing angle. The single jet shown is meant to distinguish between radio-loud (upper half) and radio-quiet (bottom half) AGN.

at z∼2-3 (Madau & Dickinson 2014), a time referred to as Cosmic Noon. Marking a critical phase of galactic activity, Cosmic Noon provides a unique opportunity to investigate SMBH growth, specifically in the context of SMBH-galaxy co-evolution.

Rest-frame optical emission lines are powerful tracers of both star formation and AGN activity, where the relative strengths of nebular emission lines from metal ions and common hydrogen transitions are determined primarily by their source of ionization. Ionization from star-forming regions is characterized by the Balmer lines Hα and Hβ from the common hydrogen transitions n=3-2 and n=4-2, where AGN activity yields those as well as a higher incidence of metal ions' forbidden transitions. Forbidden transitions, indicated by square brackets (e.g. [O II], [O III], [Ne III], [N I], [N II], [Fe VII] and [S II]), are those that occur spontaneously where the timescale for radiative decay is shorter than that required for collisional de-excitation. Moreover, emission from forbidden transitions is stronger in lower density gas, such as the NLR of an AGN, and much weaker in star-forming regions, characterized by denser gas.

Nebular emission lines have been used in a variety of diagnostic diagrams, meant to distinguish between different modes of ionization. These diagrams are well established at z∼0. The most popular diagnostic diagrams are the Baldwin Phillips and Terlevich (BPT) diagrams (Baldwin et al. 1981; Veilleux & Osterbrock 1987), which compare ratios of forbidden to Balmer transitions. More specifically, the NII-BPT diagram plots [N II]/Hα against [O III]/Hβ. An alternative diagram, proposed by Fernandes et al. (2010) maps the rest-frame equivalent width of Hα (W$_{H\alpha}$) against [N II]/Hα. This diagram, also known as the WHAN diagram, is not as established as the BPT, yet it has the advantage of convenience as it requires fewer emission lines.

By measuring emission line properties from a sample of star-forming galaxies at z∼3, and utilizing the NII-BPT and WHAN diagnostic diagrams, we study the incidence of AGN around Cosmic Noon. Investigating SMBH growth at this pivotal time, we aim to contribute to a deeper understanding of the growth history of SMBHs, particularly in the context of their co-evolution with their host galaxies.

2. TECHNICAL BACKGROUND

We utilize spectroscopic data from the Cycle 2 JWST program GO-3426 (PI: Jones). This program employs the NIRSpec Micro-Shutter Assembly (MSA), under the slit-stepping method outlined in Barišić et al. (2024), to obtain pseudo-integral field spectroscopy of 42 star-forming galaxies around Cosmic Noon, at z∼3. These galaxies reside within the Extended Groth Strip (EGS) and were selected for z∼3 using existing photometric and some spectroscopic redshifts. The galaxy selection was further constrained by stellar mass and star formation rate (SFR), requiring $M_* \geq 10^9$ $M_\odot$ and specific SFR $\geq 10^{-9}$ $M_\odot$/yr. Mass and SFR constraints were meant to ensure galaxies were massive and luminous enough to be spatially resolved at such distances. At z∼3, the rest-optical nebular emission lines used for the BPT and other diagnostics are shifted into infrared wavelengths, relevant to this work, Hα, Hβ, [N II] and [O III] are covered by the NIRSpec F170LP filter used for observations. Where

$$z + 1 = \lambda_{observed}/\lambda_{emitted} \tag{1}$$

with $\lambda_{observed}$ and $\lambda_{emitted}$ referring to the infrared and optical wavelengths respectively.

NIRSpec MSA data were preprocessed into three-dimensional data cubes for use in this work, with two spatial and one spectral dimension. Each data cube contains about 10x40 0.08x0.08 arcsecond (∼0.6x0.6 kpc) spectral-pixels (spaxels), pictured in two dimensions as Figure 2. With this approach, we are able to isolate distinct modes of ionization on a spaxel-by-spaxel basis. However, some data cubes contain artifacts from the reduction pipeline or are contaminated by flux from surrounding sources. Therefore, not every spaxel contains flux from the z∼3 target alone. For most data cubes with contamination, the emission lines from our target are apparent, for targets 6818, 7342, 12825, and especially 13475, contamination is more significant.

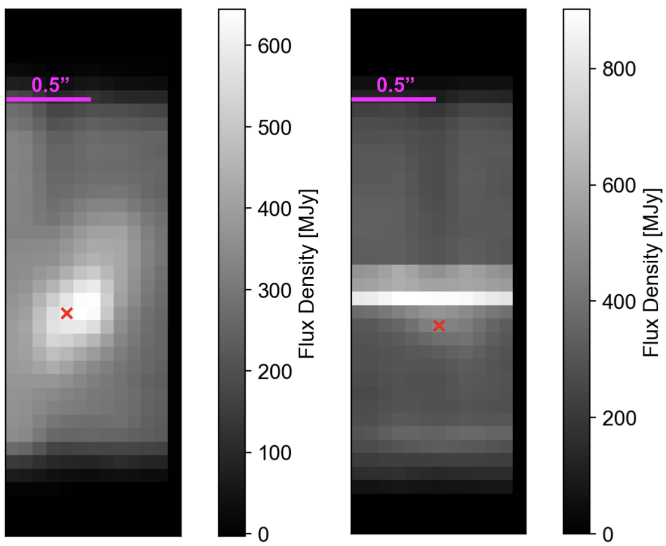

Figure 2. Two-dimensional views of the data cubes for targets 1159 (left) and 3203 (right), with integrated flux in MJy represented by intensity. The red x in each image indicates the 'central' spaxel used in fitting. The 3203 data cube highlights the artifacts and contamination we observe in our sample: the central bright line is an artifact and the fainter glow at the bottom of the cube is likely due to contamination from another source.

For each galaxy in our sample, we determine its redshift by measuring the strongest emission line observed (either Hα or [O III]), from Figure 1. We then perform multicomponent gaussian fits with a linear continuum to extract the amplitude and standard deviation (σ) of available emission lines. We find that some lines fall into gaps in wavelength coverage, due to the configuration of the MSA, as there are some discrepancies between the redshift used for selection and the true redshift of each target. We fit the Hα, [N II] and [S II] lines, followed by the Hβ and [O III] lines with 5 and 3 Gaussian1D fits from astropy (Astropy Collaboration 2022). For a given target, we ensure that all emission lines are fitted with the same width, and we fix the relative positions of these lines using their known wavelength separations. We also impose bounds on each parameter during fitting, such that they cannot be non-physical (e.g. too narrow or wide, too strong or negative, etc), and we fix the flux ratio between the lines in the [O III] and [N II] doublets to theoretical values 2.984 and 2.942.

Measuring amplitudes and standard deviations of available emission lines, we determine line ratios as relevant to the NII-BPT and WHAN diagnostics, calculate line fluxes, luminosities, velocity dispersions, and $W_{H\alpha}$ for each target. $W_{H\alpha}$ refers to the width of the box of continuum emission that is equivalent to the flux from the Hα emission line.

Some emission lines fall within our wavelength coverage, but are too faint for us to detect. With these methods, we are able to detect emission lines with fluxes as low as $\sim10^{-21-22}$ ergs $s^{-1}cm^{-2}$ per individual spaxel. This lower limit corresponds to the lowest fluxes we record in individual spaxels with above 95% confidence. Each target ID along with its RA, DEC, found redshift, and emission lines is reported in Table 1.

In order to take advantage of the spatial resolution of our data, we measure emission line properties for the entire data cube, the central 3x3 spaxels, the central spaxel, and what we call the outside cube (the entire cube excluding the central 3x3 spaxels). We define the central spaxel visually for each target, usually as the one with the strongest emission lines. As we are able to fit each individual spaxel, we are able to isolate the ionization source of the centermost spaxels in each galaxy. An example fit for the central 3x3 spaxels is shown as Figure 3 for a clearly star forming galaxy (a) and one galaxy that exhibits AGN activity (b). The ability to fit the central spaxel alone gives us a unique JWST-enabled higher detection threshold for weak AGN, those that may be overpowered by emission from star formation.

3. RESULTS AND DISCUSSION

We classify the nuclear ionization of 33 out of 42 galaxies as either driven by star formation or black hole accretion based on their emission line ratios, and corresponding placement on the BPT or WHAN diagnostic diagrams. With these classifications, we aim to quantify the growth rate of AGN at this redshift.

3.1. *AGN Incidence*

A large sample of galaxies with and without AGN activity will populate the BPT diagram in a y shape, with star-forming galaxies on the left branch and those with AGN driven activity on the right branch. This y shape is well calibrated in the z∼0 universe (Kewley et al. 2001; Kauffmann et al. 2003). Additionally, it is observationally apparent that the star-forming branch of the NII-BPT diagram evolves toward higher [N II]/Hα and [O III]/Hβ ratios at higher redshifts (e.g. Strom et al. 2017 and references within). We assemble NII-BPT diagrams for the entire, center, and outside data cubes as distinguished above. We present our measurements

Table 1. For each target in our sample, we present its ID, RA, and DEC, the redshift we determine (z), and the emission lines, relevant to the NII-BPT, that we detect. [O III] and [N II] refer to both lines in the doublet unless otherwise specified.

ID	RA	DEC	z	Emission Lines Detected
1159	214.941373	52.922763	2.625	Hα, [N II], [O III], Hβ
1952	214.926479	52.916804	3.595	Hα
1982	214.931167	52.920349	3.288	Hα, [N II], [O III], Hβ
2181	214.922492	52.915324	2.939	Hα, [N II], [O III], Hβ
2375	214.925755	52.918527	3.216	Hα, [N II], [O III], Hβ
2935	214.9137	52.913255	3.232	Hα, [O III] λ4959, Hβ
3090	214.937164	52.931031	3.383	Hα, [N II], Hβ
3173	214.923427	52.921438	3.060	Hα, [N II], [O III], Hβ
3203	214.917844	52.917769	3.230	Hα, [N II], [O III] λ4959, Hβ
3480	214.913616	52.916204	3.232	Hα, [N II], Hβ
3526	214.911379	52.914682	3.386	Hα
3823	214.922767	52.924628	3.060	Hα, [N II], [O III], Hβ
3970	214.92989	52.930387	2.918	Hα, [N II], [O III], Hβ
4233	214.916641	52.920524	3.231	Hα, Hβ
4344	214.925782	52.929975	3.210	Hα, [N II], Hβ
4517	214.927295	52.932283	3.217	Hα, [N II], Hβ
4585	214.92096	52.92797	3.059	Hα, [N II], [O III], Hβ
4598	214.918698	52.926405	2.408	Hα, [N II]
5708	214.904961	52.92241	3.217	Hα, [N II]
6352	214.914886	52.933842	3.008	Hα, [N II], Hβ
6818	214.911054	52.933124	2.212	Hα, [N II]
5011	214.905488	52.882303	3.259	Hα, [N II], [O III], Hβ
5560	214.906942	52.887432	3.219	Hα, [N II], [O III], Hβ
6275	214.9051	52.891588	3.231	Hα, [N II], [O III], Hβ
6915	214.892683	52.88736	3.442	Hα
7020	214.901466	52.894104	3.232	Hα, [O III], Hβ
7204	214.903909	52.896952	3.436	Hα, [N II], Hβ
7342	214.90398	52.898117	3.200	Hα, [N II], [O III], Hβ
7582	214.889899	52.889272	3.437	Hα, [N II]
8960	214.897326	52.902973	3.083	Hα, [N II], [O III], Hβ
9057	214.885246	52.895078	3.436	[O III], Hβ
12009	214.865875	52.898954	3.300	[O III], Hβ
12142	214.858436	52.894392	3.001	Hα, [N II], [O III], Hβ
15186	214.838038	52.898088	2.503	Hα, [N II]
15351	214.83839	52.89958	2.913	[O III], Hβ
15480	214.852082	52.909761	2.559	Hα, [N II]
12392	214.916565	52.891453	2.943	Hα, [N II], [O III], Hβ
12793	214.925415	52.913448	2.643	Hα, [N II], [O III], Hβ
12825	214.905075	52.900063	3.550	Hα
13023	214.89978	52.904568	2.573	Hα, [N II], [O III], Hβ
13458	214.865845	52.897461	2.886	Hα
13475	214.907959	52.928101	3.255*	Hα

*Redshift value may have resulted from contaminating target.

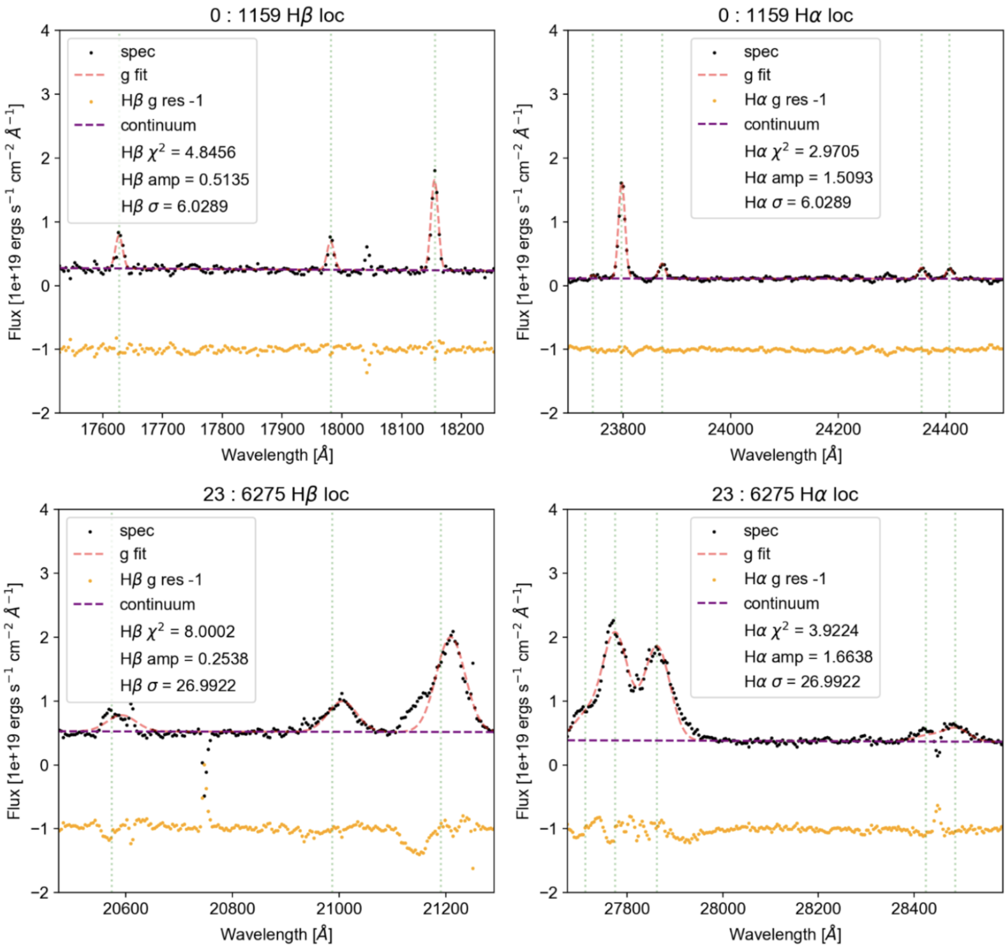

Figure 3. Gaussian fits from this work for a star-forming target (top) and a target that exhibits black hole growth (bottom). Plotting the observed wavelength in angstroms versus the integrated flux from the central 3x3 spaxels. Hβ and the [O III] complex are plotted on the left, where Hα, [N II], and [S II] are plotted on the right. Green vertical lines indicate the locations of emission lines at the found redshifts, the red and purple dashed lines indicate the overall fit and the continuum respectively, with residuals plotted as orange dots shifted -1. Values for the amplitude and standard deviation of Hα and Hβ are listed in the plot legends, along with a χ^2 value for each fit. We note a possible outflow feature in 6275's dominant [O III] line but do not investigate that in this work.

in Figure 4 along with a large sample of SDSS galaxies to show where we expect galaxies at z∼0 to fall. We plot the location of the star-forming main sequence as found for this sample of z∼0 galaxies as well as that found by Strom et al. (2017) for a sample of galaxies around z=2.31. To distinguish regionally, between star-forming and AGN-dominated ionization, we use the semi-empirically derived relation for z∼1-2.5 from Kewley et al. (2013) that marks the upper bound for the star-forming main sequence. The change in this upper bound is due to more extreme interstellar medium conditions in higher-redshift star-forming galaxies, where star formation may contribute to a higher fraction of [O III]/Hβ. We plot this relation for both z=2, in dark pink, and z=3, in light blue. Depending on our detection of emission line ratios over each (entire, center, outside) integration, we plot varying numbers of points (15, 20, 12) in red. Across all three diagrams, for those points with marginally higher (>1 dex) error, we utilize arrows instead of error bars to avoid crowding. The spaxels with the highest fluxes usually fall in the visually-identified center of each target and correspond to the strongest emission lines, explaining why we are able to plot more line ratio pairs using the integrated flux from the central 3x3 spaxels. Looking at the ratios found in the central spaxels, we have higher sensitivity to nuclear ionization. Using the integrated flux from the entire data cube (Figure 4, left) and just the outside of each data cube (Figure 4, right), it is unclear whether any of our sample exceeds the star-forming MS cut offs from Kewley. However, as we isolate the central 3x3 spaxels, where we expect any possible AGN to be located, in the central BPT, we find only one target, 6275, that lies definitively on the AGN branch of the diagram as defined by the Kewley boundary for its redshift. It is important to note that target 6275 lies much higher up on the AGN branch in the central BPT diagram as compared to the other two. When we exclude the central spaxels, in the outside BPT, the contribution from star-forming ionization is most apparent as target 6275 lies well below the Kewley boundary for its redshift.

In addition to the NII-BPT, we examine the WHAN diagram from Fernandes et al. (2010), shown in Figure 5. Fernandes et al. (2011) pose divisions in $W_{H\alpha}$ and [N II]/Hα to distinguish ionization from star formation and than from black hole growth. These divisions are posed for z∼0 and are represented by the colored boxes and labels in Figure 5. Again isolating the line ratios from the central 3x3 spaxels, and therefore isolating any AGN contribution, we are able to classify 33 of our targets using these divisions. One advantage of the WHAN diagram is that we are able to include 13 more galaxies, where we do not have the Hβ and [O III] detections requisite for the BPT. The downside to this diagram is that we do not know how to interpret its redshift evolution. It is safe to assume that the boundary between purple and green regions would be shifted toward the right, toward higher [N II]/Hα as seen with the BPT evolution toward higher redshifts, however, the extent of that shift is uncertain. That said, without accounting for redshift evolution, we find two more AGN, targets 12392 and 15480, as shown in the green strong AGN region. We note that these additional AGN detections come with less certainty than target 6275 apparent on the AGN branch in the central NII-BPT, and in the strong AGN region of the WHAN diagram.

Out of 42 galaxies, we can measure the necessary emission lines for at least one diagnostic diagram in 33 of them. Using the NII-BPT and WHAN diagrams, we detect three AGN (6275, 12392, and 15480), with 6275 being more robustly identified than the other two. That is, ∼91% of the galaxies that we can analyze, including ∼79% of our sample, seem to be exclusively star-forming. With few AGN detected, we aim to place limits on the possible AGN activity that could go undetected, as well as quantify the growth of those we identified.

3.2. *Luminosities*

The total luminous output of an AGN is directly related to the amount of material that is accreting onto it. By quantifying the luminosity from the center of each galaxy, we are able to place upper limits on the growth rate of 30 SMBHs, and estimate the growth rate for the three we detect. For the following calculations, suppose that all 33 galaxies in the 'analyzable' portion of our sample contain AGN. We assume that the flux from the NLR of any AGN is contained within the chosen central spaxel. We make this assumption because we expect any SMBH NLR to be in the central 0.1 to 1 kpc of its host galaxy. We do not account for the contribution of AGN flux outside of that central spaxel or the contamination from star formation included inside the central spaxel.

To determine the bolometric luminosity ($L_{[bol]}$) of each AGN, we utilize the most common proxy: [O III] luminosity ($L_{[OIII]}$). It is important to note that there are a range of bolometric correction (BC) factors in the literature, spanning an order of magnitude. Heckman et al. (2004) found BC=3500 using observed [O III] luminosities, where Kauffmann & Heckman (2009) found BC=600 using dust-corrected [O III] luminosities. We use the relation from Lamastra et al. (2009) in which the bolometric correction, either 87, 142, or 454 is loosely dependent on the magnitude of corrected [O III] luminosities.

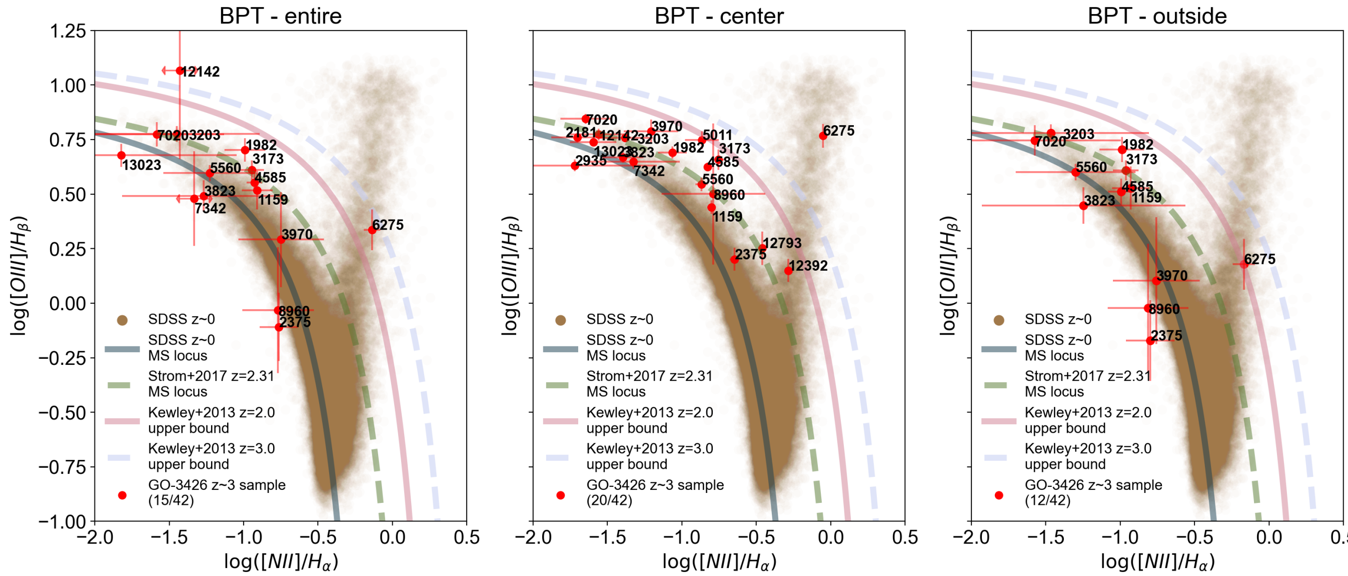

Figure 4. The NII-BPT diagrams from emission line ratios for the entire integrated data cube (left), the central 3x3 spaxels (center), and the outside data cube (right). The brown dots show a large sample of SDSS galaxies at z∼0 and the red dots show this sample at z∼3. Dark green solid and dashed lines show the location of the star-forming main sequence at z 0 and z=2.31, as presented in Strom et al. (2017). Dark pink solid and light blue dashed lines show the upper bound for main sequence star-forming galaxies at redshifts 2 and 3, using the relation from Kewley et al. (2013). It is important to note that the star-forming targets are characterized by narrower emission lines (e.g. Figure 3, top) with lower relative fluxes for forbidden transitions whereas the target on the AGN branch (6275 i.e. Figure 3, bottom) exhibits broader lines with much higher relative fluxes of forbidden transitions.

Additionally, we apply the relation from Bassani et al. (1999) to correct [O III] luminosities, where $L_{[OIII],corrected}$ is a function of $L_{[OIII]}$ and the Balmer decrement (BD). For our purposes, the BD is a ratio of Hα to Hβ, indicative of how much dust is blocking the intrinsic luminosity of each source. In cases where we calculate BD<3.0, we assume BD=3.0. 3.0 is the intrinsic BD as expected in the NLR (Osterbrock & Ferland 2006). Including only flux from the central spaxel, where the dominant [O III] emission line is available, we find corrected [O III] luminosities on the order of 10^{40} ergs s^{-1} corresponding to BC=142 from Lamastra. With this correction, we approximate bolometric luminosities on the order of 10^9 solar luminosities $L_{\odot}$. For comparison, and to note the uncertainty in these calculations, if we were to substitute the BC factor from Heckman et al. (2004) on $L_{[OIII],observed}$, we would find bolometric luminosities on the order of $10^{10.5}$ $L_{\odot}$. With generally low BD values in our sample, we use bolometric luminosities derived from the BC from Lamastra et al. (2009).

While bolometric luminosity directly corresponds to the accretion rate of a SMBH, it alone cannot tell us how much each SMBH is growing with respect to its own mass, e.g. we cannot yet quantify the SMBHs' growth rate. Therefore, a more physically meaningful way to express the rate of growth of a black hole is to compare its bolometric luminosity to its Eddington luminosity. The Eddington luminosity is a theoretical value that depends on the mass of each SMBH. It refers to the luminosity, or equivalently the accretion rate, a SMBH would emit if the force from radiation outward were to exactly counteract the pull from gravitation inward. We can approximate SMBH masses, and therefore Eddington luminosities, using measured velocity dispersions. We utilize the relation from Robertson et al. (2006) relating the stellar velocity dispersion of a host galaxy to the mass of its SMBH as

$$\log\left(M_{\rm BH}\right) = 7.72 + 4.02 \times \log\left(\frac{\sigma_{H\alpha}}{200}\right) \tag{2}$$

.

Robertson et al. (2006) report this relation with 0.26 dex uncertainty. With SMBH masses in hand, we approximate Eddington luminosities, as

$$L_{\rm Edd}\,[{\rm erg\,s^{-1}}] = 1.26 \times 10^{38}\, M_{\rm BH}\,[M_{\odot}] \tag{3}$$

.

We plot bolometric luminosities derived from $L_{[OIII],corrected}$ against Eddington luminosities derived from $\sigma_{H\alpha}$ as Figure 6.

3.3. *Eddington Ratios*

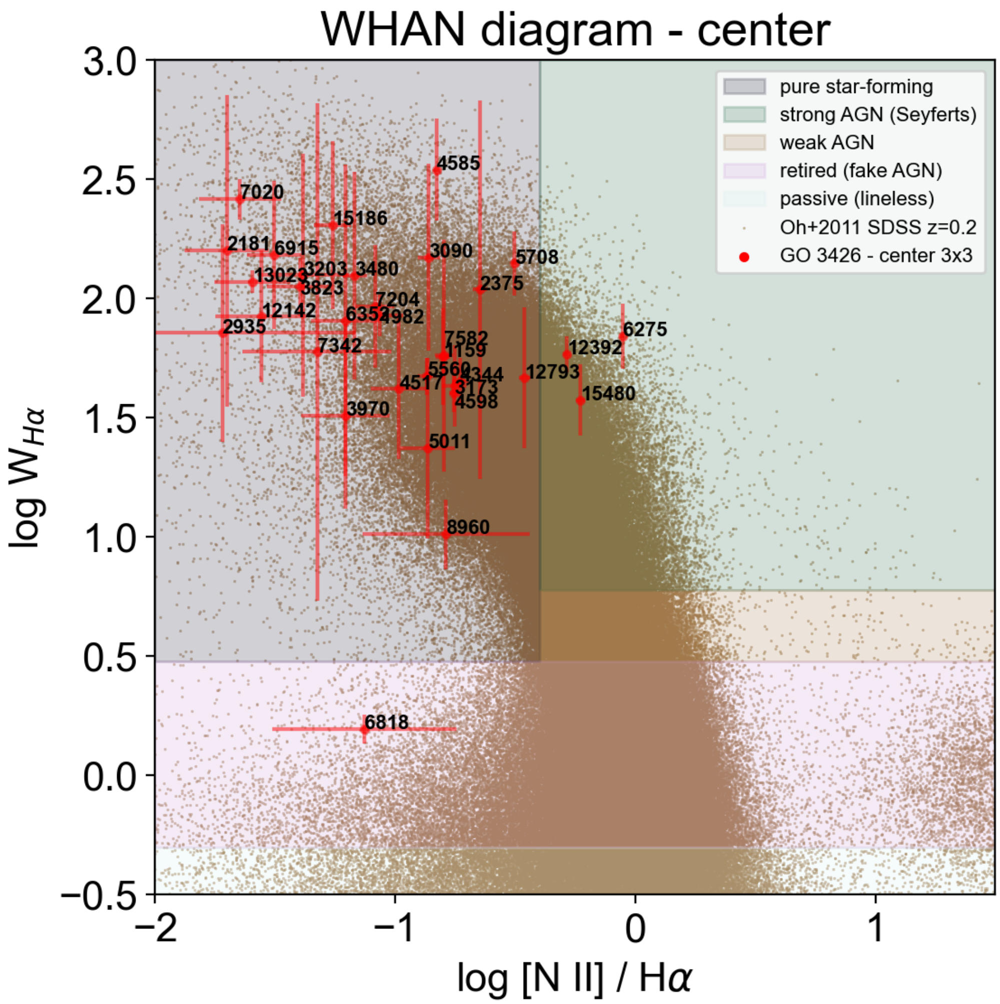

Figure 5. WHAN diagram for this sample. Plotting $W_{H\alpha}$ against [N II]/Hβ for the integrated flux from the central 3x3 spaxels for 33/42 targets. Colored boxes distinguish different ionizing sources based on emission line ratios.

The ratio of the bolometric luminosity to the Eddington luminosity is called the Eddington ratio, denoted by λ. Aggarwal (2024) and references therein report that the typical Eddington ratios for AGN have both mass and redshift dependence, where higher mass, and lower redshift AGN correspond to lower Eddington ratios. For example, below z$\sim$0.3, Schulze & Wisotzki (2010) find an average value of $\lambda\sim$0.1, where above z=5.7, Shen et al. (2019) find an average Eddington ratio of 0.3. As another point for comparison, Lamastra et al. (2009) find $\lambda\sim$0.1 for broad line AGN between z$\sim$0.3-0.4.

In our sample, we find a median Eddington ratio of 0.01, such that if the galaxies in our sample truly have SMBH that are growing, they are doing so at an underwhelming rate. Out of the three galaxies where we detect AGN, we are able to determine Eddington ratios for two of them, as the stronger [O III] line is not present in one. For those two targets, the Eddington ratios correspond to physical values, where the others reflect upper limits. We plot the Eddington ratio as a function of SMBH mass, as a fraction of stellar mass, as Figure 7. We note two distinct outliers, targets 5011 and 3203, that we attribute to possible underestimation of SMBH mass, although further investigation is necessary to refine those measurements. It is important to note that we find very low SMBH mass fractions as compared to Suh et al. (2020) who report an average fraction of 0.03 for z<2.5. However, for our purposes, underestimating SMBH masses would make our upper limits on Eddington ratios higher, not compromising this work.

Aggarwal (2024) report that for any given redshift, higher mass black holes are characterized by lower Eddington ratios, with which our result is consistent. We note that the relationships we are using in each step of determining the Eddington ratios come with a lot of uncertainty.

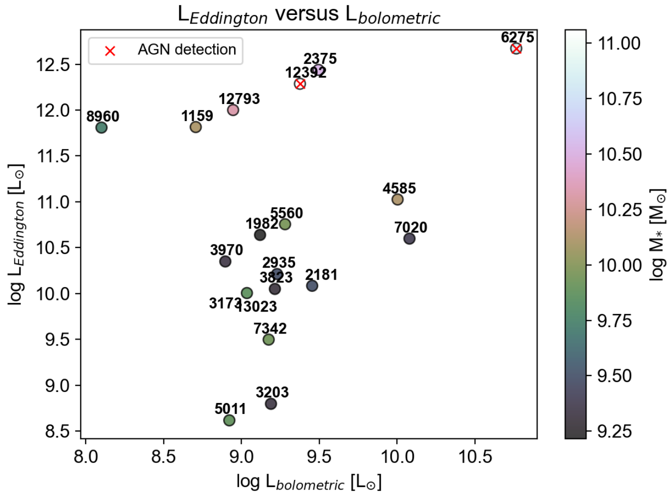

Figure 6. Approximations (for detected AGN), and upper limits for Eddington luminosities derived from SMBH masses and bolometric luminosities from corrected [O III] luminosity. Although there is no apparent trend in this plot, it is important to note that the targets with detected AGN correspond to the highest Eddington luminosities and stellar masses.

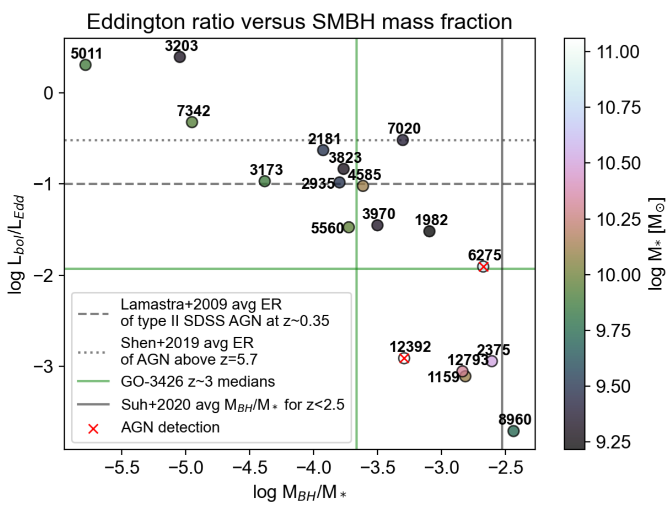

Figure 7. Eddington ratios for targets that exhibit AGN, marked with x's, and Eddington ratio upper limits for those targets marked with points, plotted against SMBH mass as a fraction of stellar mass. We plot the median Eddington ratio from our sample as well as the values found for AGN at z∼0.35 and at z>5.6 by Lamastra et al. (2009) and Shen et al. (2019) as horizontal lines. We plot the average black hole mass fraction from our sample as well as the value found by Suh et al. (2020) for AGN at z<2.5 for comparison.

4. CONCLUSION

From our sample of star-forming galaxies at z∼3, where we expect the height of star formation and black hole growth associated with Cosmic Noon, we detect very few AGN. Using the BPT and WHAN diagnostic diagrams, for galaxies with requisite emission lines, we identify only three targets that host AGN. Of these, 6275 falls within the AGN region on both diagrams, while 12392 and 15480 are classified as AGN based solely on the WHAN diagram, not accounting for its possible redshift evolution.

For two of the three identified AGN, we are able to estimate bolometric luminosities, black hole masses, and Eddington luminosities, and thus approximate their Eddington ratios. We also place upper limits on Eddington ratios for an additional 18 galaxies. We find a median Eddington ratio around 1%, indicating that the AGN that we do detect are growing at 1% of their Eddington limits, a very small fraction of their total mass. For the galaxies where no AGN are detected, it is likely that the black holes are accreting at even lower rates.

Our lack of strong AGN detections could mean a few different things in the context of SMBH evolution and SMBH-galaxy co-evolution. It is possible that the star formation in most of these galaxies is using up the cold gas that would otherwise be accreting onto the black hole, making star formation and heightened AGN activity mutually exclusive. It is also possible that this cosmic time is simply characterized by weak AGN that are growing at $\leq 1\%$ of their Eddington limits. Either way, even accounting for large uncertainty in our Eddington ratio calculations, it is apparent that the majority of our sample does not harbor rapidly growing SMBHs as might be expected at z∼3. On the other hand, this low AGN incidence is consistent with that reported by Genzel et al. (2014) for z∼2, where higher mass galaxies are much more likely to host AGN. Interestingly, those galaxies where we do detect AGN lie in the top 10% of masses in this sample. Therefore, although lower mass SMBH are suspected to grow at higher rates, only the higher mass SMBH are actually growing at this redshift. That said, our Eddington ratio approximations indicate SMBHs at this time are growing at a rate far lower than their Eddington limits. This result suggests that any, but especially lower mass, SMBHs are not growing at z∼3. With a median SMBH mass of 10^6 $M_\odot$ for our sample, it is possible that SMBHs have finished growing by this time.

Future work is necessary as we intend to further compare our investigation to relevant literature on SMBH-galaxy co-evolution. We would also like to better constrain the star formation rates of this sample to analyze how their star formation compares to larger samples of galaxies with both active and inactive nuclei. This route could lend insight into the mechanisms of co-evolution if higher star formation rates could correspond with lower SMBH growth rates. It may also be possible to more robustly distinguish between star-forming and AGN modes of ionization in our sample, as we could potentially include more targets by using different emission line combinations, like the MEx and KEx diagrams.

REFERENCES

Aggarwal, Y. 2024, MNRAS, 530, 1512, doi:10.1093/mnras/stae914.

Alexander, E. 2022, AstroVis-v0.1.0, Zenodo, doi:10.5281/ZENODO.5899326.

Astropy Collaboration, Price-Whelan, A. M., Lim, P. L., et al. 2022, ApJ, 935, 167, doi:10.3847/1538-4357/ac7c74.

Baldwin, J. A., Phillips, M. M., Terlevich, R. 1981, PASP, 93, 5, doi:10.1086/130766.

Begelman, M. C., Volonteri, M., Rees, M. J. 2006, MNRAS, 370, 289, doi:10.1111/j.1365-2966.2006.10467.x.

Bromm, V., Loeb, A. 2003, ApJ, 596, 34, doi:10.1086/377529.

Cid Fernandes, R., Stasińska, G., Mateus, A., et al. 2011, MNRAS, 413, 1687, doi:10.1111/j.1365-2966.2011.18244.x.

Cid Fernandes, R., Stasińska, G., Schlickmann, M. S., et al. 2010, MNRAS, 403, 1036, doi:10.1111/j.1365-2966.2009.16185.x.

Fan, X., Bañados, E., Simcoe, R. A. 2023, ARA&A, 61, 373, doi:10.1146/annurev-astro-052920-102455.

Ferrarese, L., Merritt, D. 2000, ApJ, 539, L9, doi:10.1086/312838.

Gebhardt, K., Bender, R., Bower, G., et al. 2000, ApJ, 539, L13, doi:10.1086/312840.

Genzel, R., Schreiber, N. M. F., Rosario, D., et al. 2014, ApJ, 796, 7, doi:10.1088/0004-637X/796/1/7.

Inayoshi, K., Visbal, E., Haiman, Z. 2020, ARA&A, 58, 27, doi:10.1146/annurev-astro-120419-014455.

Kauffmann, G., Heckman, T. M., Tremonti, C., et al. 2003, MNRAS, 346, 1055, doi:10.1111/j.1365-2966.2003.07154.x.

Kewley, L. J., Dopita, M. A., Sutherland, R. S., et al. 2001, ApJ, 556, 121, doi:10.1086/321545.

Kewley, L. J., Maier, C., Yabe, K., et al. 2013, ApJ, 774, L10, doi:10.1088/2041-8205/774/1/L10.

Kormendy, J., Ho, L. C. 2013, ARA&A, 51, 511, doi:10.1146/annurev-astro-082708-101811.

Kormendy, J., Richstone, D. 1995, ARA&A, 33, 581, doi:10.1146/annurev.aa.33.090195.003053.

Madau, P., Dickinson, M. 2014, ARA&A, 52, 415, doi:10.1146/annurev-astro-081811-125615.

Madau, P., Rees, M. J. 2001, ApJ, 551, L27, doi:10.1086/319848.

Magorrian, J., Tremaine, S., Richstone, D., et al. 1998, AJ, 115, 2285, doi:10.1086/300353.

McKee, C. F., Tan, J. C. 2008, ApJ, 681, 771, doi:10.1086/587434.

Montero, P. J., Janka, H.-T., Müller, E. 2012, ApJ, 749, 37, doi:10.1088/0004-637X/749/1/37.

Osterbrock, D. E., Ferland, G. J. 2006, Astrophysics of Gaseous Nebulae and Active Galactic Nuclei.

Rees, M. J. 1978, MNRAS, 77, 237.

Strom, A. L., Steidel, C. C., Rudie, G. C., et al. 2017, ApJ, 836, 164, doi:10.3847/1538-4357/836/2/164.

Suh, H., Civano, F., Trakhtenbrot, B., et al. 2020, ApJ, 889, 32, doi:10.3847/1538-4357/ab5f5f.

Tan, J. C., McKee, C. F. 2004, arXiv:astro-ph/0403498.

Urry, C. M., Padovani, P. 1995, PASP, 107, 803, doi:10.1086/133630.

Veilleux, S., Osterbrock, D. E. 1987, ApJS, 63, 295, doi:10.1086/191166.

Volonteri, M. 2010, A&A Rv, 18, 279, doi:10.1007/s00159-010-0029-x.

Zhuang, M.-Y., Ho, L. C. 2023, Nature Astronomy, 7, 1376, doi:10.1038/s41550-023-02051-4.